

Improving cyclability of Li metal batteries at elevated temperatures and its origin revealed by cryo-electron microscopy

Jiangyan Wang^{1,3}, William Huang^{1,3}, Allen Pei^{1,3}, Yuzhang Li¹, Feifei Shi¹, Xiaoyun Yu¹ and Yi Cui^{1,2*}

Operations of lithium-ion batteries have long been limited to a narrow temperature range close to room temperature. At elevated temperatures, cycling degradation speeds up due to enhanced side reactions, especially when high-reactivity lithium metal is used as the anode. Here, we demonstrate enhanced performance in lithium metal batteries operated at elevated temperatures. In an ether-based electrolyte at 60 °C, an average Coulombic efficiency of 99.3% is obtained and more than 300 stable cycles are realized, but, at 20 °C, the Coulombic efficiency drops dramatically within 75 cycles, corresponding to an average Coulombic efficiency of 90.2%. Cryo-electron microscopy reveals a drastically different solid electrolyte interface nanostructure emerging at 60 °C, which maintains mechanical stability, inhibits continuous side reactions and guarantees good cycling stability and low electrochemical impedance. Furthermore, larger lithium particles grown at the elevated temperature reduce the electrolyte/electrode interfacial area, which decreases the per-cycle lithium loss and enables higher Coulombic efficiencies.

Lithium-ion batteries (LIBs) have revolutionized energy storage and become the state-of-the-art secondary battery technology for portable electronics and electric vehicles^{1,2}. However, the practical operating temperature of LIBs is normally limited to between 0 and 45 °C (refs. ^{3,4}). As the temperature drops below 0 °C, the reversible battery capacity is reduced as a result of the increased electrolyte viscosity, large polarization and slow interfacial kinetics^{5–9}. In addition, it is widely acknowledged that cycling stability degrades at elevated temperatures due to the increased reactivity of the electrode materials and consequent side reactions, namely severe solid electrolyte interphase (SEI) formation^{10–15}. Accordingly, optimal performance in LIBs is usually achieved between 15 and 35 °C (Fig. 1)¹⁶. Additionally, with the ever growing demand for high energy density, anode materials with even higher reactivities, such as Li metal, are being researched and implemented. Li metal is the ultimate anode for lithium-based batteries, with the lowest electrode potential (−3.04 V versus standard hydrogen electrode) and highest theoretic capacity (3,860 mAh g^{−1}) of all possible candidates^{17–19}. However, the thermally induced degradation and accelerated aging of Li metal batteries is expected to be exacerbated due to its low electrode potential and consequent high reactivity^{20,21}.

In this Article, we show that, despite its high reactivity, Li metal displays an anomalously high Coulombic efficiency (CE) and long-term cycling stability at 60 °C compared to that at 20 °C in an ether-based electrolyte. The CE of Cu/Li cells reaches ~99% for the 10th cycle and stably cycles at 99–99.8% for over 300 cycles at 60 °C, while the CE drops to 79.7% after only 75 cycles at 20 °C. We note that an improved cycling performance in Li–S batteries has been reported at high current densities²²; this was explained by a change in Li dendrite morphology as a result of the generated local heat. Here, much enhanced performance is achieved at an elevated cell operating temperature; importantly, this originates from a completely different

SEI-based mechanism. Specifically, cryo-electron microscopy (cryo-EM) reveals an amorphous polymeric SEI formed at 20 °C, which is soluble in the electrolyte and fractures during cycling, thus offering limited passivation of the Li metal and leading to continuous SEI formation and mechanical instability. Conversely, a highly ordered layered SEI is formed at 60 °C, which effectively passivates the anode and maintains mechanical stability during cycling, thus inhibiting later-cycle SEI formation and leading to much better cycling stability. It is worth noting that an adverse effect of high temperature is observed in additive-free carbonate electrolytes: the SEI remains as an amorphous interphase with embedded inorganic nanoparticles at both 20 and 60 °C, but at 60 °C the SEI grows thicker and Li dendrites become non-uniform, inducing worse cycling stability. We also demonstrate the beneficial effect of high-temperature operation in an ether-based electrolyte using LiFePO₄/Li cells; at a C-rate of 20C, a reversible capacity of 131 mAh g^{−1} is achieved at 60 °C, compared to 61 mAh g^{−1} at 20 °C. The reduced SEI formation with larger Li particles formed at elevated temperature as well as smaller and more stable impedance can further enhance the performance at elevated temperature.

Enhanced performance demonstrated by Cu/Li cells

To study the effect of temperature on battery performance, Li foil was paired with Cu foil in a coin cell configuration. An ether-based electrolyte was adopted that consisted of 1.0 M lithium bis-trifluoromethanesulfonylimide (LiTFSI) in 1:1 vol/vol 1,3-dioxolane/1,2-dimethoxyethane (DOL/DME) with 1% lithium nitrate (LiNO₃) (by weight) additive (termed DOL/DME/LiNO₃ electrolyte).

Our major finding is that the CE of Cu/Li cells cycled at a higher temperature is superior to the CE for those cycled at a lower temperature (Fig. 2a). At a current density of 1 mA cm^{−2} and with a deposition capacity of 1 mAh cm^{−2}, the first cycle CEs of cells cycled

¹Department of Materials Science and Engineering, Stanford University, Stanford, CA, USA. ²Stanford Institute for Materials and Energy Sciences, SLAC National Accelerator Laboratory, Menlo Park, CA, USA. ³These authors contributed equally: Jiangyan Wang, William Huang, Allen Pei
*e-mail: yicui@stanford.edu

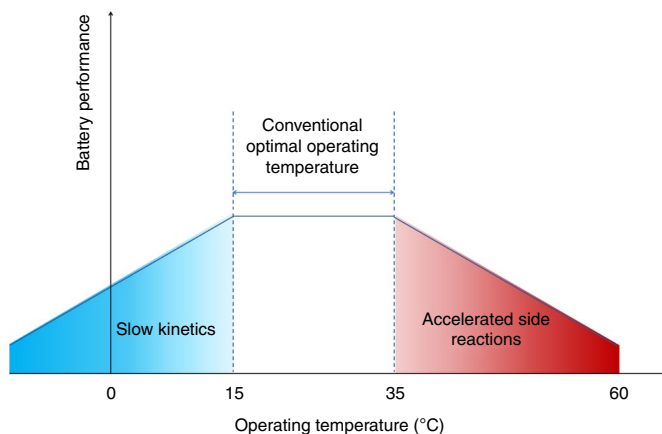


Fig. 1 | The conventional wisdom about the operating temperature of battery performance. As the operating temperature drops below 0 °C, the reversible battery capacity is reduced due to increased electrolyte viscosity and slower interfacial kinetics. At elevated temperatures, cycling stability degrades due to aggravated side reactions and severe SEI formation. As a result, desirable performance is achieved within an operating temperature range of 15–35 °C.

at 60, 20, 0 and -20°C are 97.6, 97.4, 96.1 and 65.4%, respectively. For the cells cycled at -20°C , the CE drops to 27% at the second cycle, and remains around 30% thereafter. For cells cycled at 0 °C, the CE drops gradually to 58% at the 30th cycle, while a CE of 92.8% is retained after 51 cycles for the cells cycled at 20 °C. For the cells cycled at 60 °C, the CE reaches ~99% for the 10th cycle and remains at 99.4% for the 51st cycle. Moreover, Cu/Li cells cycled at 60 °C exhibited a much improved long-term cycling stability compared to those cycled at 20 °C (Fig. 2b); the CE at 60 °C remained high at 99–99.8% for over 300 cycles, while the CE at 20 °C dropped to 79.7% after only 75 cycles. In addition, the voltage hysteresis between the Li plating and stripping voltage plateaux decreases as the temperature is increased (Fig. 2c,d and Supplementary Fig. 1), which is attributed to the lower polarization and faster charge transport kinetics at elevated temperature (Supplementary Figs. 2 and 3). Even at an ultra-high current density of 20 mA cm^{-2} and a high areal capacity of 20 mAh cm^{-2} , the cells cycled at 60 °C still maintain a CE of 98.8% after 30 cycles (Supplementary Fig. 4).

Cryo-EM characterization

To elucidate the nanoscopic changes leading to the much enhanced CE and cycling stability at high temperatures, we studied the morphological features of the Li metal particle and its SEI formed at 20 °C and 60 °C using cryo-EM. Although the SEI is crucial to the initial capacity loss, long-term cycling and rate capability of Li batteries, it is poorly understood because of the complexity of the chemical/electrochemical reactions involved in its formation and the lack of techniques to explore its physical properties^{23,24}. In previous studies^{25–27}, cryo-EM techniques were developed to characterize the detailed structure of the Li metal and its SEI, demonstrating that atomic-resolution imaging of sensitive battery materials in their native state is possible and that battery performance depends intimately on the SEI nanostructure.

Li metal grows as spherical particles in the DOL/DME/LiNO₃ electrolyte system. The size of the Li metal particles deposited at 60 °C is larger than those deposited at 20 °C (Fig. 3a,e), which could be attributed to the smaller overpotential and faster charge transfer at higher temperature. Similarly, due to the enhanced reaction kinetics at elevated temperature, a thicker SEI layer is formed at 60 °C than at 20 °C (35 nm versus 20 nm) (Fig. 3b,f). In addition,

a distinct SEI nanostructure emerges at elevated temperature; while the SEI formed at 20 °C consists of an amorphous, polymeric interphase (Fig. 3c,d), the SEI formed at 60 °C possesses an inverse layered nanostructure (Fig. 3g,h), similar to that proposed by others^{25,28}. Although the innermost layer consists of an amorphous polymer matrix, the enhanced kinetics at high temperature results in large grains of crystalline Li₂O (~10 nm) at the outer interface with the liquid electrolyte. The boundaries between the Li₂O layer, polymeric interface and Li metal are clearly observed in high-resolution cryo-EM image (Supplementary Fig. 5).

The organic components in the amorphous polymeric SEI formed at 20 °C are soluble in the electrolyte, resulting in poor anode passivation and a high probability of fracture. This leads to continuous side reactions and SEI formation, which is manifested in a low CE and poor cycling stability^{29,30}. In contrast, the SEI formed at 60 °C has a thicker and more ordered multilayered structure, which makes it mechanically robust and stable during cycling, while also more effectively passivating the anode^{30,31}. As a result, the cells cycled at 60 °C achieved much higher CEs and a more stable cycling life than those cycled at 20 °C.

Morphology and size distribution analysis

In addition to differences in SEI nanostructure, we also observe an increased size of Li metal particles with increased deposition temperature. Figure 4a–i shows the morphology of Li particle nuclei deposited in a wide temperature window from -20 to 60°C at a rate of 0.25 mA cm^{-2} with a capacity of 0.15 mAh cm^{-2} . This low areal capacity is equivalent to a Li metal thin film of ~750 nm and allows us to analyse the particle size distribution. At temperatures below 0 °C, the Li metal nuclei are small and densely packed. The dimpled shape of the particles is a result of the inevitable exposure to ambient atmosphere during sample transfer to the scanning electron microscope (SEM) chamber³². As the deposition temperature increases, the Li nuclei increase in size and are sparsely distributed on the Cu substrate. These nuclei are less spherical and fuse together, which may be ascribed to pressing by the separator³². The non-uniformity of these agglomerated particles deposited at a temperature over 30 °C makes it difficult to analyse their individual size distribution, so data for temperatures of 40, 50 and 60 °C are not presented in the following statistical data. The distributions of Li particle sizes deposited at different temperatures are clearly illustrated through the histograms in Fig. 4j, which exhibit an approximately Gaussian distribution (the particle size varies within a narrow size distribution due to heterogeneity in the electrode) and demonstrate the increase of Li particle size as the deposition temperature is increased.

Increased Li nuclei size at elevated temperatures is due to decreased polarization and overpotential. As shown in Fig. 4k, both the nucleation overpotential ($-\eta_n$, nucleation of Li embryos, below 0 V versus Li/Li⁺) and the plateau overpotential ($-\eta_p$, Li nuclei growth) decrease with increasing deposition temperature. The critical nuclei radius is related to the deposition overpotential by the following equation^{32,33}:

$$r = 2YV_m/(F |\eta_n|) \quad (1)$$

where r is the lithium nucleus radius, Y is the surface energy of the Li/electrolyte interface, V_m is the molar volume of Li, F is Faraday's constant and η_n is the nucleation overpotential. We observe an inverse relationship between nuclei size and overpotential, which is well supported by Fig. 4l. The larger Li particles nucleated at 60 °C reduce the unfavourable electrode/electrolyte contact area, inhibit side reactions and SEI formation, resulting in less irreversible Li consumption and a higher CE. The coupling of increased particle size with increased temperature is an additional contribution to enhanced performance of Li batteries in DOL/DME/LiNO₃ electrolyte at elevated temperatures.

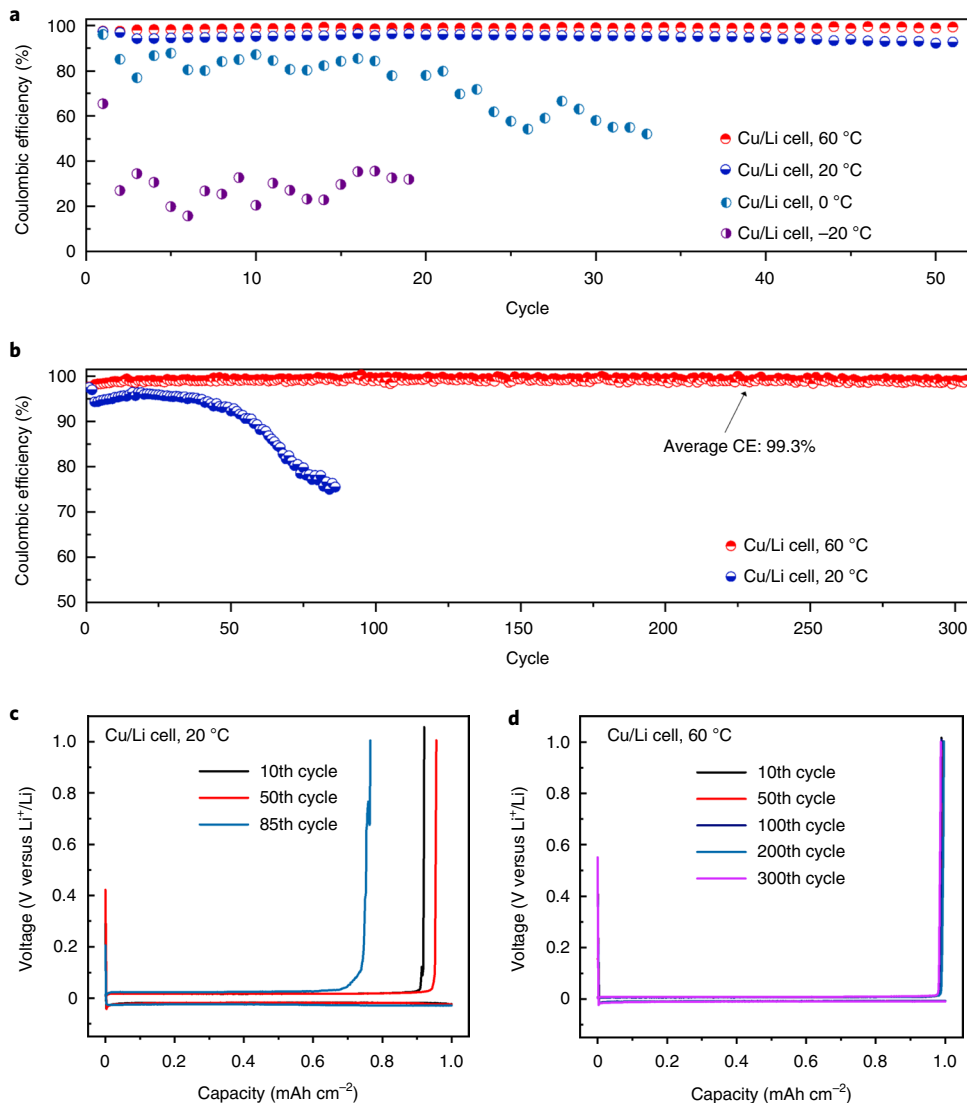


Fig. 2 | Enhanced performance at elevated temperature demonstrated by Cu/Li cells. All Cu/Li cells were cycled in DOL/DME/LiNO₃ electrolyte using 1M LiTFSI salt. **a**, CE of Cu/Li cells cycled at -20, 0, 20 and 60 °C, respectively, at a current density of 1 mA cm⁻² and a deposition capacity of 1 mAh cm⁻². **b**, Long-term cycling of Cu/Li cells at 20 and 60 °C. **c,d**, Voltage profiles of different cycles for Cu/Li cells cycled at 20 °C (**c**) and 60 °C (**d**).

Impedance evolution analysis

The enhanced electrochemical performance at elevated temperature is also corroborated by electrochemical impedance spectroscopy (EIS) (Fig. 5). All EIS was carried out with Li stripped to a voltage of 1 V versus Li⁺/Li. The equivalent circuit model of the impedance spectra is shown in Fig. 5a, where R_s reflects the combined resistance of the electrolyte, separator and electrodes, R_{SEI} and C_{SEI} are the resistance and capacitance of the SEI layer, which corresponds to the high-frequency semicircle, R_{ct} and C_{dl} are the charge transfer resistance and double-layer capacitance, corresponding to the medium frequency semicircle, and Z_w is the Warburg impedance attributed to the combined effect of Li ions diffusing across the electrode–electrolyte interface, which appears as a sloped line in the low-frequency region.

The calculated resistance (which includes both R_{SEI} and R_{ct}) after various cycles at different temperatures is shown in Fig. 5c,f. Evidently, the resistance decreases as the temperature increases, showing 224, 134, 32 and 7 Ω, respectively after the first cycle for the cells operated at -20, 0, 20 and 60 °C. We attribute the lower resistance at higher temperatures to decreased electrolyte viscosity,

which enables better electrode/electrolyte contact, weaker polarization and lower energy barriers for ion transfer³⁴. As supported by Fig. 2c,d and Supplementary Fig. 1, cells operated at 60 °C demonstrate the smallest voltage hysteresis between lithiation and delithiation, demonstrating low polarization and enhanced kinetics. In addition, the resistances of all cells increase after cycling for 100 cycles (cells operated at -20 °C failed after 25 cycles) with the exception of those operated at 60 °C. Cell resistances increase by 191% after 25 cycles for the cells operated at -20 °C (cells fail after 25 cycles, so the impedance data thereafter are not presented), while resistance increases of 56 and 28% were obtained after 100 cycles for cells operated at 0 and 20 °C. Conversely, for cells operated at 60 °C, the resistance decreases slightly from 7 Ω to 5.5 Ω after the fifth cycle, and becomes stable after 50 cycles (4.2 and 4 Ω after the 50th and 100th cycle).

The continuous increase in cell resistance during cycling at 20 °C and below contrasts with the stable cell resistance at 60 °C, which agrees well with the above observed improved CE and cycling stability at elevated temperature (Fig. 2 and Supplementary Figs. 6 and 7). This enhancement can be explained by the improved

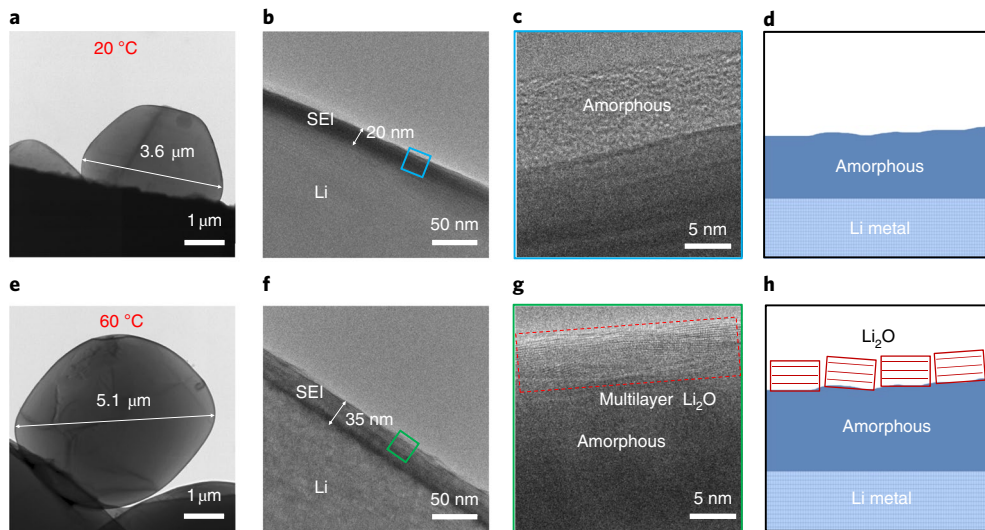


Fig. 3 | Cryo-EM reveals an emergent SEI nanostructure formed at elevated temperature. **a–h**, Li metal was deposited in DOL/DME/LiNO₃ electrolyte using 1 M LiTFSI salt at 20 °C (**a–d**) and 60 °C (**e–h**) at a rate of 1 mA cm⁻² with a capacity of 0.4 mAh cm⁻²; cryo-EM images of Li metal particles showing the particle size (**a,e**); cryo-EM images of the SEI interface showing the SEI thickness (**b,f**); magnified images of the blue region (**c**) outlined in **b** and the green region (**g**) outlined in **f**, showing the structure of the SEI interface; schematics of the observed amorphous SEI structure on a Li particle grown at 20 °C (**d**) and a thicker layered SEI nanostructure on a Li particle grown at 60 °C (**h**).

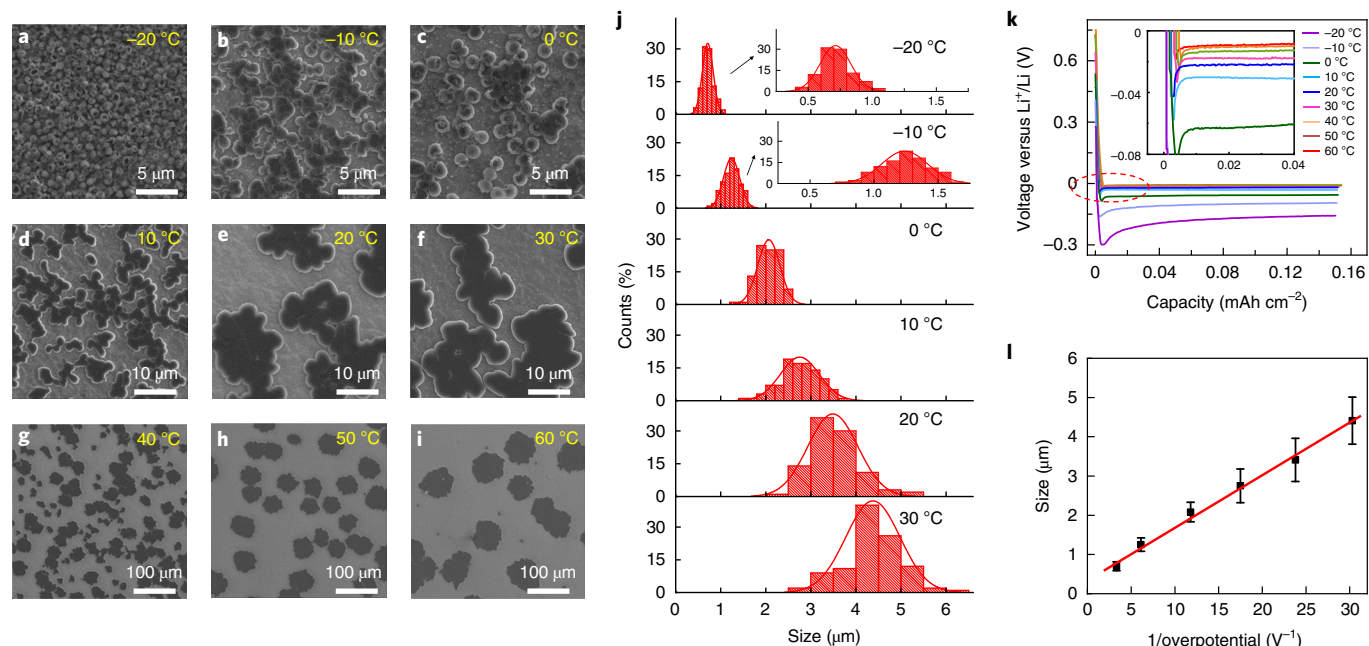


Fig. 4 | Elevated temperature nucleates larger Li particles and optimizes the electrode/electrolyte contact area. Li particles were deposited on a Cu substrate in DOL/DME/LiNO₃ electrolyte using 1 M LiTFSI salt under various temperatures at a current density of 0.25 mA cm⁻² with a capacity of 0.15 mAh cm⁻². **a–i**, SEM images of Li metal particles deposited at -20 °C (**a**), -10 °C (**b**), 0 °C (**c**), 10 °C (**d**), 20 °C (**e**), 30 °C (**f**), 40 °C (**g**), 50 °C (**h**) and 60 °C (**i**). **j**, Histograms of Li metal particle size distribution after deposition at different temperatures. Inset: enlarged images of histograms of particle deposition at -20 °C and -10 °C. The superimposed line shows a fitted Gaussian distribution. **k**, Voltage profiles of deposition at various temperatures. Inset: enlarged image of the red circled region to show the nucleation plateau more clearly. **l**, Plot of Li metal particle size versus inverse overpotential of Li deposition. The average size (black dots) and standard deviation (size variation, error bars) were calculated with statistics of the sizes of ~150 particles using Origin software. Red line, linear relationship between particle size and inverse overpotential.

kinetics at high temperature and optimization in the SEI nanostructure³⁵. First, the much enhanced electrochemical kinetics at higher temperatures (Arrhenius-type kinetics) facilitates Li ion redox and decreases the charge-transfer resistance, which is consistent with the

EIS results observed for cells operated at 60 °C (ref. ³⁶). Second, the amorphous SEI polymer matrix formed at a low temperature tends to dissolve into electrolyte and easily fractures during lithiation /delithiation cycling. The repeated SEI breakdown/repair induces

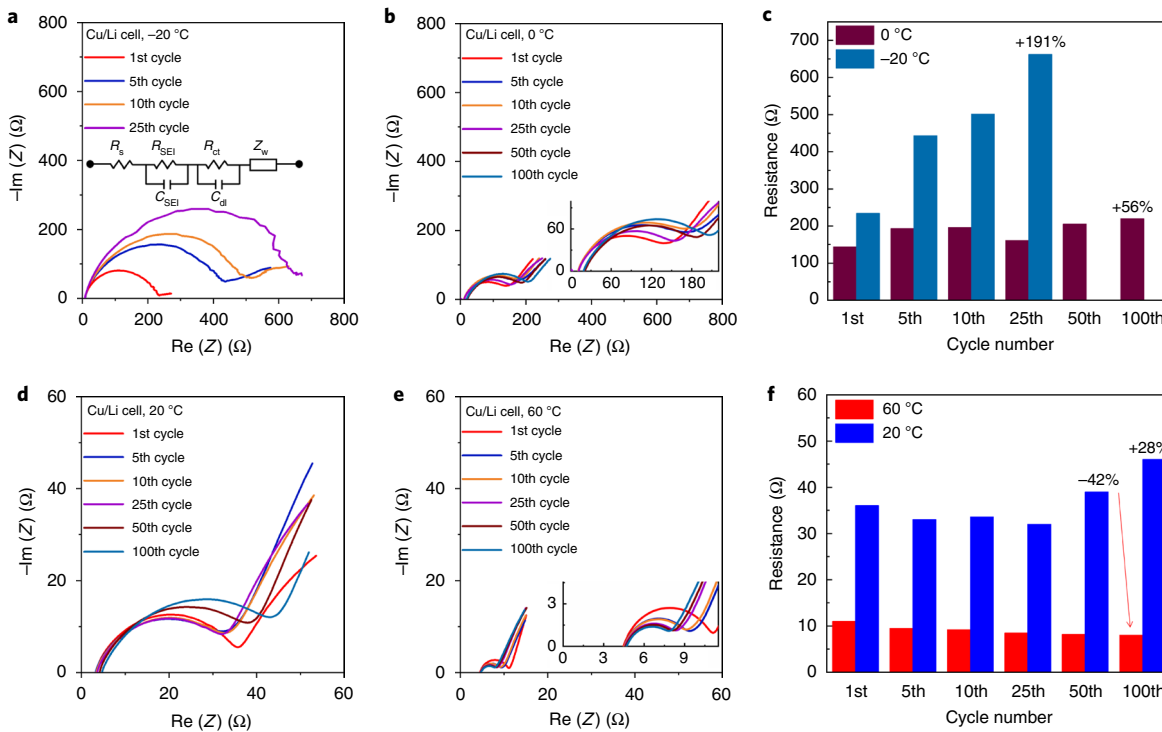


Fig. 5 | Elevated temperature results in small and stable impedance during cycling. **a,b,d,e**, Impedance spectra of the Li metal anode cycled at $-20\text{ }^{\circ}\text{C}$ (**a**), $0\text{ }^{\circ}\text{C}$ (**b**), $20\text{ }^{\circ}\text{C}$ (**d**) and $60\text{ }^{\circ}\text{C}$ (**e**) for various cycles in DOL/DME/LiNO₃ electrolyte using 1 M LiTFSI salt, carried out after delithiation to a voltage of 1 V versus Li⁺/Li. Inserted in **a** is the equivalent circuit scheme for interpretation of the impedance spectra. **c,f**, Two-dimensional plots showing the impedance change at different cycles operated at $-20\text{ }^{\circ}\text{C}$ and $0\text{ }^{\circ}\text{C}$ (**c**) and $20\text{ }^{\circ}\text{C}$ and $60\text{ }^{\circ}\text{C}$ (**f**).

continuous side reactions and SEI formation, resulting in increased resistance, decreased CE and poor stability, as observed in cells operated at -20 , 0 and $20\text{ }^{\circ}\text{C}$. Conversely, the SEI formed at $60\text{ }^{\circ}\text{C}$ is thicker and possesses an organic/inorganic composite layered structure, enabling it to fully passivate the surface and remain mechanically stable during cycling, inhibiting later-cycle SEI formation. As a result, the cell operated at $60\text{ }^{\circ}\text{C}$ exhibits a decreased resistance, enhanced CE and cycling stability.

Temperature effect in other electrolyte systems

To fully study the effect of temperature, the electrochemical performances of Cu/Li cells in three other electrolytes were tested at 20 and $60\text{ }^{\circ}\text{C}$. The electrolytes were 1.0 M LiTFSI in 1:1 vol/vol DOL/DME (named as DOL/DME electrolyte) without LiNO₃, 1.0 M LiPF₆ in 1:1 vol/vol ethylene carbonate and diethyl carbonate (EC/DEC) without or with 10% fluoroethylene carbonate (FEC) (by volume) additive (named EC/DEC and EC/DEC/FEC, respectively).

The results demonstrate that high temperature leads to a beneficial effect on electrochemical performance in the DOL/DME or EC/DEC/FEC electrolyte systems, similar to that in DOL/DME/LiNO₃ electrolyte, while an adverse effect is observed in EC/DEC electrolyte (Supplementary Figs. 8 and 9). We attribute these divergent results to the following two effects. First, although all SEI interfaces become thicker at a higher temperature, their structures evolve differently as temperature elevates (Supplementary Fig. 10). In DOL/DME electrolyte, the SEI structure remains as an amorphous, polymeric interphase as the temperature increases. In EC/DEC electrolyte, the SEI structure consists of an amorphous, polymeric interphase with inorganic nanoparticles embedded inside at both $20\text{ }^{\circ}\text{C}$ and $60\text{ }^{\circ}\text{C}$. In comparison, the outer inorganic layer of SEI formed in EC/DEC/FEC electrolyte becomes much thicker at $60\text{ }^{\circ}\text{C}$ than at $20\text{ }^{\circ}\text{C}$, which makes the SEI more robust and mechanically stable during cycling.

As a result, a higher CE and better cycling stability are achieved at a higher temperature in EC/DEC/FEC electrolyte. Second, all lithium nuclei in these three kinds of electrolyte show whisker-like or dendritic growth at $20\text{ }^{\circ}\text{C}$ (Supplementary Fig. 11). As the temperature increases to $60\text{ }^{\circ}\text{C}$, the Li dendrites in DOL/DME electrolyte grow much larger and form island-like morphologies by fusing multiple nuclei together during growth. The larger size and island-like morphology decrease the electrode/electrolyte contact area, thus inhibiting SEI formation and resulting in an enhanced performance at $60\text{ }^{\circ}\text{C}$ in DOL/DME electrolyte. In EC/DEC electrolyte, the Li dendrites become very non-uniform at $60\text{ }^{\circ}\text{C}$, which induces an uneven impedance and current density distribution, and thus poorer cycling stability. Similar to DOL/DME and DOL/DME/LiNO₃ electrolytes, the enhanced Li dendrite size formed in EC/DEC/FEC electrolyte at a higher temperature further benefits the battery performance. However, the still obvious dendritic growth of Li in EC/DEC/FEC electrolyte at elevated temperature limits the improvement in CE. Therefore, the beneficial effect of high temperature is insignificant in EC/DEC/FEC electrolyte (Supplementary Fig. 12).

Enhanced performance demonstrated by LiFePO₄/Li cells

To further demonstrate the beneficial effect of elevated temperature on battery performance, Li foil was paired with a traditional LiFePO₄ cathode (LiFePO₄:conductive carbon (Super P):polyvinylidene fluoride (PVDF)=80:10:10 by weight) using DOL/DME/LiNO₃ electrolyte in a coin cell configuration. The advantage of LiFePO₄ over other cathode materials is the high thermal stability of LiFePO₄ and good compatibility with various electrolytes³⁷.

As shown in Fig. 6c,d, the difference between the lithiation and delithiation voltage plateaus at $60\text{ }^{\circ}\text{C}$ is decreased relative to $20\text{ }^{\circ}\text{C}$ (0.05 versus 0.10 V at 1C, 0.27 versus 0.43 V at 20C, where $1\text{C}=170\text{ mA g}^{-1}$), benefitting from the lower polarization and faster

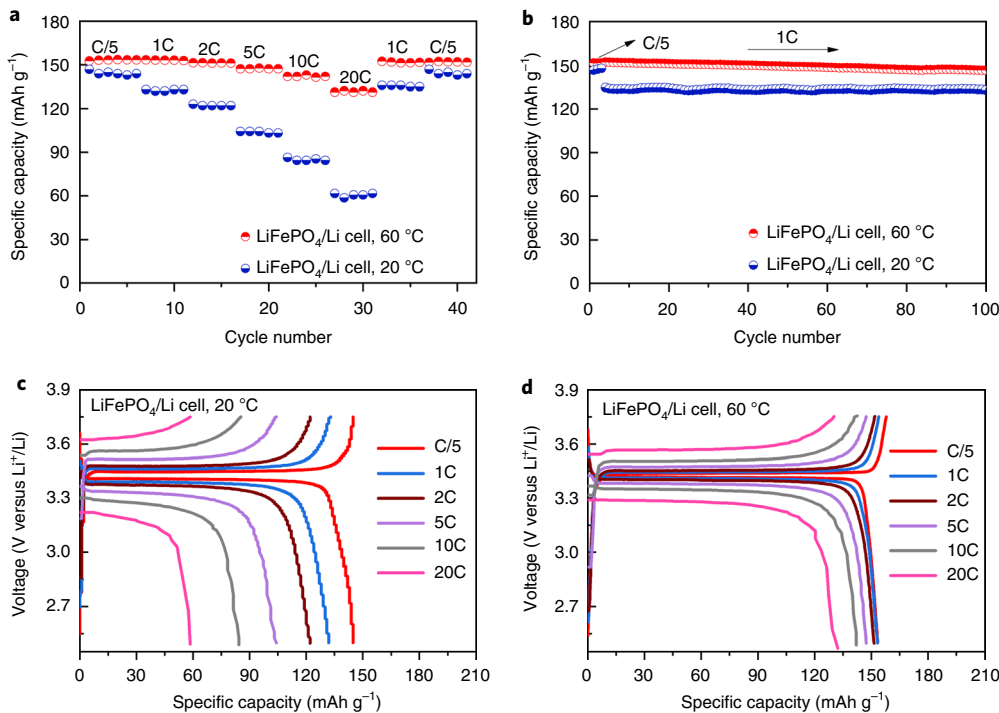


Fig. 6 | Enhanced performance at elevated temperature demonstrated by LiFePO₄/Li cells. All LiFePO₄/Li cells were cycled in DOL/DME/LiNO₃ electrolyte using 1M LiTFSI salt. **a**, Rate capability of LiFePO₄/Li cells cycled at various C-rates from 0.2C to 20C (1C=170 mA g⁻¹) with a voltage range of 2.5–3.75 V, at 20 and 60 °C. **b**, Long-term cycling of LiFePO₄/Li foil cells cycled at 0.2C for the first three cycles and 1C for the following cycles at 20 and 60 °C. **c,d**, Voltage profiles of LiFePO₄/Li cells cycled at various C-rates from 0.2C to 20C at 20 °C (**c**) and 60 °C (**d**).

charge transport kinetics at higher temperature. As a result, the capacities of LiFePO₄/Li cells operated at 60 °C are much higher than those at 20 °C, with stark differences at high C-rate (142 versus 86 mAh g⁻¹ at 10C, 131 versus 61 mAh g⁻¹ at 20C, Fig. 6a). In addition, the cycling stability of LiFePO₄/Li cells, which is limited by the CE of the Li metal anode, can be enhanced at elevated temperature. At an intermediate C-rate of 1C, cells exhibited good cycling stability of 146 mAh g⁻¹ after 100 cycles for 60 °C, compared to 133 mAh g⁻¹ after 100 cycles at 20 °C (Fig. 6b). The good cycling stability of LiFePO₄/Li cells operated at 60 °C is attributed to the improved CE of the Li metal anode at elevated temperature, as demonstrated above. Our findings differ from the conventional viewpoint that performance is poor at high temperature; rather, we observe that battery operation at elevated temperature improves the CE and cycling stability, especially at high C-rates.

Conclusions

In summary, we have shown that high-temperature battery operation can lead to a favourable SEI nanostructure, enlarge Li particle size and provide faster kinetics, resulting in enhanced CE and cycling stability. The CE reaches as high as 99.8% and remains stable for over 300 cycles in DOL/DME/LiNO₃ electrolyte. Cryo-EM characterization reveals an organic/inorganic composite layered SEI formed at 60 °C, distinct from the amorphous polymeric SEI formed at 20 °C. This emergent SEI maintains mechanical stability during cycling and effectively passivates the Li surface, leading to long-term cycling stability. Synergistically, Li particle size enlarges as the temperature elevates, which reduces the unfavourable electrolyte/electrode interfacial area, resulting in less SEI formation and higher CEs. Impedance evolution analysis demonstrates that impedance decreases with increasing temperature and remains stable during cycling at 60 °C, which further illustrates the enhanced performance achieved at high temperature. This present work

challenges conventional viewpoints on thermal considerations in battery operation and provides a fundamental insight into the effect of temperature on battery performance, widening the operational environments and applications of Li batteries.

Methods

Electrochemistry. LiFePO₄ cathode films were prepared using a conventional slurry method. LiFePO₄ powders, carbon black conductive additive (Super P, TIMCAL) and polyvinylidene fluoride (PVDF, Kynar HSV 900) binder, with a mass ratio of 8:1:1 were dispersed in N-methyl-2-pyrrolidone (NMP) and stirred overnight. The obtained homogeneous dispersion was doctor-bladed on high-purity Al foil and dried at 60 °C in a vacuum oven for over 12 h. Films were then calendered and cut into 1 cm² circular disks. The mass loading of the LiFePO₄ cathode was about 14–15 mg cm⁻². In an Ar-filled glovebox, working electrodes were assembled into Type 2032 coin cells with a polymer separator (Celgard 2250) and Li metal foil (0.75 mm thick, 99.9%, Alfa Aesar) as the counter/reference electrode. A 75 µl volume of 1.0 M LiTFSI in 1:1 vol/vol DOL/DME with 1% LiNO₃ (by weight) additive was added as the electrolyte. For the Cu/Li cell, bare Cu foil replaced LiFePO₄ films as the working electrode, while the other processes remained the same. Four electrolytes were used: 1.0 M LiTFSI in 1:1 vol/vol DOL/DME with/without 1% LiNO₃ (by weight) additive, and 1.0 M LiPF₆ in 1:1 vol/vol EC/DEC with/without 10% FEC (by volume) additive. Coin cells were loaded into a battery tester (Land Instruments) and cycled between 2.5 and 3.75 V (LiFePO₄/Li cell). For Cu/Li cells, Li metal with an areal capacity of 1, 3 or 20 mAh cm⁻² was deposited onto the working electrode by applying a current of 1, 3 or 20 mA cm⁻² for 1 h.

Cryo-transfer procedure. To prepare the cryo-EM sample, coin cells were assembled using 300-mesh Cu transmission electron microscopy (TEM) grids as the working electrode. After Li metal was deposited on the TEM grid, cells were immediately disassembled in the glovebox and TEM grids were washed with 1,3-dioxolane to remove Li salts. Once dry, the TEM grid with plated Li was placed in an Eppendorf tube and transferred out of the glovebox. The positive pressure inside the Ar-filled glovebox (and thus the Eppendorf tube) prevented air from leaking into the tube. The sealed Eppendorf tube was plunged quickly into a bath of liquid nitrogen (LN₂), then quickly crushed with a bolt cutter while still immersed in the LN₂ to expose the Li metal to the cryogen. The TEM grid then carefully mounted onto a TEM cryo-holder (Gatan 626)

using a cryo-transfer station to ensure this entire process occurred under LN₂ immersion. During insertion into the TEM column (~1 s), a built-in shutter on the holder was closed to prevent contact of Li with air, while a LN₂ dewar attached to the holder maintained the sample at cryogenic temperature. In this way, the reactive battery material could be safely transferred from the coin cell to the TEM without any chance of reaction with ambient air. Once inside the TEM column, the sample was kept cold at -178 °C.

Materials characterization. All cryogenic TEM characterizations were carried out using an FEI Titan 80–300 environmental (scanning) TEM operated at an accelerating voltage of 300 kV. The instrument was equipped with an aberration corrector in the objective lens, which was tuned before each sample analysis. Other characterizations were carried out using SEM (FEI Sirion, Nova NanoSEM) and EIS (BioLogic VMP3). All samples were rinsed with DOL and dried inside the glovebox before microscopy.

Data availability

The data that support the plots within this paper and other findings of this study are available from the corresponding author upon reasonable request.

Received: 22 November 2018; Accepted: 16 May 2019;

Published online: 01 July 2019

References

- Tarascon, J. M. & Armand, M. Issues and challenges facing rechargeable lithium batteries. *Nature* **414**, 359–367 (2001).
- Chu, S. & Majumdar, A. Opportunities and challenges for a sustainable energy future. *Nature* **488**, 294–303 (2012).
- Leng, F., Tan, C. M. & Pecht, M. Effect of temperature on the aging rate of Li ion battery operating above room temperature. *Sci. Rep.* **5**, 12967 (2015).
- Lithium Ion Rechargeable Batteries: Technical Handbook* (Sony Corporation, 2009); <https://cdn.sparkfun.com/datasheets/Prototyping/Lithium%20Ion%20Battery%20MSDS.pdf>
- Cho, H.-M., Choi, W.-S., Go, J.-Y., Bae, S.-E. & Shi, H.-C. A study on time-dependent low temperature power performance of a lithium-ion battery. *J. Power Sources* **198**, 273–280 (2012).
- Zhang, S. S., Xu, K. & Jow, T. R. Electrochemical impedance study on the low temperature of Li-ion batteries. *Electrochim. Acta* **49**, 1057–1061 (2004).
- Sides, C. R. & Martin, C. R. Nanostructured electrodes and the low-temperature performance of Li-ion batteries. *Adv. Mater.* **17**, 125–128 (2005).
- Ishikawa, M., Kanemoto, M. & Morita, M. Control of lithium metal anode cycleability by electrolyte temperature. *J. Power Sources* **81–82**, 217–220 (1999).
- Yang, X.-G., Zhang, G., Ge, S. & Wang, C.-Y. Fast charging of lithium-ion batteries at all temperatures. *Proc. Natl Acad. Sci. USA* **115**, 7266–7271 (2018).
- Yan, P. et al. Tailoring grain boundary structures and chemistry of Ni-rich layered cathodes for enhanced cycle stability of lithium-ion batteries. *Nat. Energy* **3**, 600–605 (2018).
- Ramadass, P., Haran, B., White, R. & Popov, B. N. Capacity fade of Sony 18650 cells cycled at elevated temperatures Part I. Cycling performance. *J. Power Sources* **112**, 606–613 (2002).
- Liu, D.-Q., Liu, X.-Q. & He, Z.-Z. The elevated temperature performance of LiMn₂O₄ coated with Li₄Ti₅O₁₂ for lithium ion battery. *Mater. Chem. Phys.* **105**, 362–366 (2007).
- Shim, J., Kostecki, R., Richardson, T., Song, X. & Striebel, K. A. Electrochemical analysis for cycle performance and capacity fading of a lithium-ion battery cycled at elevated temperature. *J. Power Sources* **112**, 222–230 (2002).
- Waldmann, T., Wilka, M., Kasper, M., Fleischhammer, M. & Wohlfahrt-Mehrens, M. Temperature dependent ageing mechanisms in lithium-ion batteries—a post-mortem study. *J. Power Sources* **262**, 129–135 (2014).
- Jung, H.-G., Jang, M. W., Hassoun, J., Sun, Y.-K. & Scrosati, B. A high-rate long-life Li₄Ti₅O₁₂/Li[Ni_{0.45}Co_{0.1}Mn_{1.45}]O₄ lithium-ion battery. *Nat. Commun.* **2**, 516 (2011).
- Schimpe, M. et al. Comprehensive modeling of temperature-dependent degradation mechanisms in lithium iron phosphate batteries. *J. Electrochem. Soc.* **165**, A181–A193 (2018).
- Xu, W. et al. Lithium metal anodes for rechargeable batteries. *Energy Environ. Sci.* **7**, 513–537 (2014).
- Tikekar, M. D., Choudhury, S., Tu, Z. & Archer, L. A. Design principles for electrolytes and interfaces for stable lithium-metal batteries. *Nat. Energy* **1**, 16114 (2016).
- Lin, D., Liu, Y. & Cui, Y. Reviving the lithium metal anode for high-energy batteries. *Nat. Nanotechnol.* **12**, 194–206 (2017).
- Xu, K. Nonaqueous liquid electrolytes for lithium-based rechargeable batteries. *Chem. Rev.* **104**, 4303–4417 (2004).
- Xu, K. Electrolytes and interphases in Li-ion batteries and beyond. *Chem. Rev.* **114**, 11503–11618 (2014).
- Li, L. et al. Self-heating-induced healing of lithium dendrites. *Science* **359**, 1513–1516 (2018).
- Winter, M. The solid electrolyte interphase—the most important and the least understood solid electrolyte in rechargeable Li batteries. *Z. Phys. Chem.* **223**, 1395–1406 (2009).
- Wang, A., Kadam, S., Li, H., Shi, S. & Qi, Y. Review on modeling of the anode solid electrolyte interphase (SEI) for lithium-ion batteries. *npj Comput. Mater.* **4**, 15 (2018).
- Li, Y. et al. Atomic structure of sensitive battery materials and interfaces revealed by cryo-electron microscopy. *Science* **358**, 506–510 (2017).
- Li, Y. et al. Correlating structure and function of battery interphases at atomic resolution using cryo-electron microscopy. *Joule* **2**, 2167–2177 (2018).
- Zachman, M. J., Tu, Z., Choudhury, S., Archer, L. A. & Kourkoutis, L. F. Cryo-STEM mapping of solid–liquid interfaces and dendrites in lithium-metal batteries. *Nature* **560**, 345–349 (2018).
- Aurbach, D., Ein-Ely, Y. & Zaban, A. The surface chemistry of lithium electrodes in alkyl carbonate solutions. *J. Electrochem. Soc.* **141**, L1–L3 (1994).
- Mogensen, R., Brandell, D. & Younesi, R. Solubility of the solid electrolyte interphase (SEI) in sodium ion batteries. *ACS Energy Lett.* **1**, 1173–1178 (2016).
- Pan, H. et al. Addressing passivation in lithium–sulfur battery under lean electrolyte condition. *Adv. Funct. Mater.* **0**, 1707234 (2018).
- Mikhaylik, Y. V. Electrolytes for lithium sulfur cells. US patent 7,354,680 B2 (2008).
- Pei, A., Zheng, G., Shi, F., Li, Y. & Cui, Y. Nanoscale nucleation and growth of electrodeposited lithium metal. *Nano Lett.* **17**, 1132–1139 (2017).
- Ely, D. R. & Garcia, R. E. Heterogeneous nucleation and growth of lithium electrodeposits on negative electrodes. *J. Electrochem. Soc.* **160**, A662–A668 (2013).
- Wang, F.-M. et al. Aging effects to solid electrolyte interface (SEI) membrane formation and the performance analysis of lithium ion batteries. *Int. J. Electrochem. Sci.* **6**, 1014–1026 (2011).
- Liu, Y. et al. An artificial solid electrolyte interphase with high Li-ion conductivity, mechanical strength, and flexibility for stable lithium metal anodes. *Adv. Mater.* **29**, 1605531 (2017).
- Tu, Z. et al. Nanoporous hybrid electrolytes for high-energy batteries based on reactive metal anodes. *Adv. Energy Mater.* **7**, 1602367 (2017).
- Hu, Q. et al. Graft copolymer-based lithium-ion battery for high-temperature operation. *J. Power Sources* **196**, 5604–5610 (2011).

Acknowledgements

Y.C. acknowledges support from the Assistant Secretary for Energy Efficiency and Renewable Energy, Office of Vehicle Technologies, Battery Materials Research (BMR) Program and Battery 500 Consortium of the US Department of Energy, Stanford Global Climate and Energy Projects (GCEP), the Office of Naval Research, the Joint Center for Energy Storage Research (JCESR) and a KAUST Investigator Award. A.P. acknowledges support from the National Defense Science and Engineering Graduate Fellowship and the Stanford Graduate Fellowship. Part of this work was performed at the Stanford Nano Shared Facilities (SNSF), supported by the National Science Foundation under award ECCS-1542152.

Author contributions

J.W., A.P. and Y.C. conceived and designed the experiments. J.W. and A.P. performed the experiments. W.H. and Y.L. conducted TEM characterization. J.W., A.P., W.H. and Y.C. co-wrote the paper. All authors discussed the results and commented on the manuscript.

Competing interests

The authors declare no competing interests.

Additional information

Supplementary information is available for this paper at <https://doi.org/10.1038/s41560-019-0413-3>.

Reprints and permissions information is available at www.nature.com/reprints.

Correspondence and requests for materials should be addressed to Y.C.

Publisher's note: Springer Nature remains neutral with regard to jurisdictional claims in published maps and institutional affiliations.

© The Author(s), under exclusive licence to Springer Nature Limited 2019